Journal of Power Sources 186 (2009) 115–122

Contents lists available at ScienceDirect

Journal of Power Sources

journal homepage: www.elsevier.com/locate/jpowsour

Ultra-thin nanocrystalline lanthanum strontium cobalt ferrite ($La_{0.6}Sr_{0.4}Co_{0.8}Fe_{0.2}O_{3-\delta}$) films synthesis by RF-sputtering and temperature-dependent conductivity studies

Bo-Kuai Lai, Alex C. Johnson, Hui Xiong, Shriram Ramanathan*

Harvard School of Engineering and Applied Sciences, Harvard University, Cambridge, MA 02138, USA

ARTICLE INFO

Article history:
Received 18 August 2008
Received in revised form
22 September 2008
Accepted 23 September 2008
Available online 4 October 2008

Keywords:
Lanthanum strontium cobalt ferrite
Yttria-stabilized zirconia
Solid oxide fuel cell
Cathode
Ultra-thin film
Nanocrystalline

ABSTRACT

Nanocrystalline lanthanum strontium cobalt ferrite (LSCF) ultra-thin films with high in-plane electrical conductivity have been deposited by RF sputtering from composite targets. The films, with nominal thickness of 54 nm, are crystalline when annealed or deposited at temperatures above 450 °C. Effects of annealing temperature, annealing time, and substrate temperature on crystallization, microstructure, and room temperature lateral electrical conductivity have been systematically studied. No interfacial reaction products between the LSCF and single crystalline yttria-stabilized zirconia (YSZ) were observed from X-ray diffraction studies upon annealing until 750 °C. In-plane electrical conductivity as high as 580 S cm^{-1} at 650 °C has been observed for LSCF thin films deposited on single crystalline YSZ substrates and sputtered nanocrystalline YSZ thin films; while activation energy for conductivity were determined to be 0.15 eV and 0.10 eV for the former and latter films, respectively, in 650–400 °C range. The high in-plane electrical conductivity for the nanocrystalline LSCF ultra-thin films is likely attributed to their low level of porosity. Micro-solid oxide fuels cells using 15 nm thick LSCF films as cathodes and sub-100 nm yttria-doped zirconia thin film electrolytes have been fabricated successfully and demonstrated to achieve peak power density of 60 mW cm^{-2} at 500 °C. Our results demonstrate that RF sputtering provides a low-temperature synthesis route for realizing ultra-thin nanocrystalline LSCF films as cathodes for intermediate- or low-temperature solid oxide fuel cells.

1. Introduction

With increasing demand for energy coupled with finite reserve of fossil fuels and coals, it is imperative to develop sustainable, alternative energy sources. Hydrogen (or hydrocarbon)-fueled solid oxide fuel cells (SOFCs), with energy efficiency higher than 60% and clean emissions, represents a promising energy alternative [1]. They can be used in stationary power plants to replace coals and in automobiles to replace gasoline [2]. By taking advantage of well-established microfabrication techniques, low-cost micro-SOFCs (μSOFCs) for portable electronics have also stimulated considerable attention [3–6].

The hurdles that have yet to overcome for current SOFCs development are their high temperature operation (>900 °C) and, consequently, high cost and long-term durability issues [7]. To lower operation temperature, cathodes need special attention because they are responsible for majority of voltage loss in SOFCs [8,9]. Three approaches have usually been pursued to improve cathode performance at low temperatures: (i) using new cathode materials to replace conventional lanthanum strontium manganite (LSM) – which does not provide sufficient ionic conductivity below 800 °C [10–12]; (ii) using thinner cathode layer to reduce Ohmic resistance [11,12]; and (iii) using nanocrystalline microstructures to enhance oxygen-ion diffusion through the cathode via grain boundaries [13].

Lanthanum strontium cobalt ferrite (LSCF) has long been considered as one of the most promising cathode materials [14] for low-temperature operation due to its high mixed ionic and electronic conductivities and high electrocatalytic activity of oxygen reduction reaction that occurs on entire cathode surfaces rather than only at three phase boundaries. As a result, thin dense films could provide comparable or higher cathode performance than conventional thick porous films [15,16]. However, there are several technological and fundamental challenges for realizing LSCF thin film cathodes for SOFCs. Firstly, most of synthesis methods for LSCF thin films involve high temperature treatment (>800 °C) [13,17,18] that may lead to resistive interfacial reaction products, such as $La_2Zr_2O_7$ and $SrZrO_3$, with yttria-stabilized zirconia (YSZ) – one

* Corresponding author.
E-mail address: shriram@seas.harvard.edu (S. Ramanathan).

0378-7753/$ – see front matter © 2008 Elsevier B.V. All rights reserved.
doi:10.1016/j.jpowsour.2008.09.094

of the most widely used electrolytes in SOFCs [19]. For example, it has been reported that in $La_{0.9}Sr_{0.1}MnO_3$-YSZ systems, thickness of $La_2Zr_2O_7$ reaction layer could be as high as 25 nm when treated only at 700 °C [19]. Therefore, the formation of resistive reaction layers is of particular concern for ultra-thin LSCF films when their thickness may become comparable to that of the reaction layer. Although interfacial reactions between LSCF and YSZ can be avoided by using gadolinia-doped ceria (GDC) as an interlayer [20], GDC suffers from stability in highly reducing environment [19].

Secondly, since most of the LSCF thin films that have been studied are thicker than 1 μm, it is still not well understood how LSCF thin films behave at nanoscale [4,13] and whether they could be as conductive as their bulk counterparts [14,21]. Gauckler and co-workers have recently reported on synthesis of thin-film LSCF and their transport properties [4,6,13]. Although enhanced electrochemical performance has been reported for the $La_{0.52}Sr_{0.48}Co_{0.18}Fe_{0.82}O_{3-\delta}$ ultra-thin films deposited by pulsed laser deposition [13], electrical conductivity of $La_{0.6}Sr_{0.4}Co_{0.2}Fe_{0.8}O_{3-\delta}$ films, deposited by spray pyrolysis, that are more than one order of magnitude lower than their bulk counterpart casts concerns of possible degradation of material performance as cathodes due to nanosize effect and nanocrystallinity [4]. Finally, if LSCF were to be used for μSOFCs, a deposition technique that is compatible with Si-based microfabrication and appropriate post-deposition treatments of as-deposited thin films need to be developed [3,22].

In this report, we presented a systematic, detailed study on RF-sputtered $La_{0.6}Sr_{0.4}Co_{0.8}Fe_{0.2}O_{3-\delta}$ ultra-thin films. To the best of authors' knowledge, although sputtering has been widely used to deposit multi-component oxides, no prior reports of sputtering of LSCF thin films exist or any data on their high temperature conductivity have been reported so far. Further, there has been no prior study on ultra-thin $La_{0.6}Sr_{0.4}Co_{0.8}Fe_{0.2}O_{3(\delta}$ films to our knowledge. Our choice of $La_{0.6}Sr_{0.4}Co_{0.8}Fe_{0.2}O_{3(\delta}$ composition for this study is partly due to their higher electronic and ionic conductivities, lower activation energy of electronic and ionic conduction [14,21,23,24], and, significantly lower activation energy for oxygen surface exchange [15] – all as a result of higher cobalt content. A main factor that prefers $La_{0.6}Sr_{0.4}Co_{0.2}Fe_{0.8}O_{3(\delta}$ over $La_{0.6}Sr_{0.4}Co_{0.8}Fe_{0.2}O_{3(\delta}$ – namely, its thermal expansion mismatch with YSZ, as well as with silicon (Si) – can be partially mitigated by low heat treatment temperature and controlling their thickness and will be discussed in a later section.

Some key aspects of this paper are to demonstrate that $La_{0.6}Sr_{0.4}Co_{0.8}Fe_{0.2}O_{3(\delta}$ ultra-thin films exhibiting (i) no interfacial reaction products of $La_2Zr_2O_7$ ad $SrZrO_3$ between LSCF and YSZ, (ii) nanocrystalline microstructures, and (iii) high in-plane electrical conductivities can be realized by RF sputtering from a $La_{0.6}Sr_{0.4}Co_{0.8}Fe_{0.2}O_{3(\delta}$ composite target. Furthermore, we will demonstrate functional μSOFCs that utilize ultra-thin LSCF films as cathodes. Our results indicate that the LSCF ultra-thin films could be well-suited for intermediate- or low-temperature SOFC cathodes and RF sputtering provides a relatively low-temperature, microfabrication-compatible route for LSCF thin films synthesis [21].

2. Experimental procedure

RF sputtering was carried out using a custom $La_{0.6}Sr_{0.4}C_{0.8}F_{0.2}O_3$ target (from AJA International) at a gun power of 60 W. Base and Ar plasma pressure of sputtering chamber were 3×10^{-8} Torr and 5×10^{-3} Torr, respectively. Two different substrates with typical dimension of 10 mm × 10 mm × 0.5 mm were used, including (i) yttria-stabilized zirconia (YSZ) (1 0 0) substrates, and (ii) 75 nm YSZ films – sputtered from a 8% yttria-doped zirconia (from AJA International) at a gun power of 100 W and a pressure of 5×10^{-3} Torr – on 200 nm Si_3N_4 coated Si (1 0 0) substrates. Annealing was performed in ambient in a Thermolyne 21100 tube furnace. Annealing time was 2 h unless otherwise specified. Grazing incidence X-ray diffraction (XRD) and X-ray reflectivity (XRR) measurements were performed with a Scintag 2000 diffractometer using Cu Kα radiation. Microstructures were investigated by Veeco NanoMan VS atomic force microscopy (AFM) in a class 100 cleanroom and Carl Zeiss Ultra 55 field emission scanning electron microscopy (SEM). Lateral electrical conductivity at room temperature was measured by a Creative Design Engineering ResMap 168 four-point probe resistivity mapping system. High temperature lateral electrical conductivity was obtained by performing van der Pauw measurement in a home-built high temperature furnace system with an alumina sample holder and electrical assembly. Silver paste was used as the electrode contacts on four corners of the thin film samples. Four platinum leads were attached to the electrodes for independent current and voltage measurements. Further details of our high temperature probe station can be found elsewhere [25].

3. Results and discussion

To investigate crystallization behavior and to elucidate the correlation between microstructure and conductivity, sputtering was initially performed on single crystalline YSZ substrates without substrate heating. The films (referred to as LSCF/sc-YSZ thin films) were then annealed from 350 °C at every 50 °C increment until 750 °C to investigate the crystallization process. XRD was taken after every annealing step. Fig. 1 shows evolution of the diffraction patterns taken from the as-deposited amorphous LSCF films, with thickness of 54 nm, on YSZ single crystalline substrates upon sequential annealing. As seen in Fig. 1, the films were amorphous when annealed at 400 °C. After annealing at 450 °C, a peak appears at ~33.1° (2-theta). Peaks at ~23.1°, ~40.7° and ~47.2° also appear

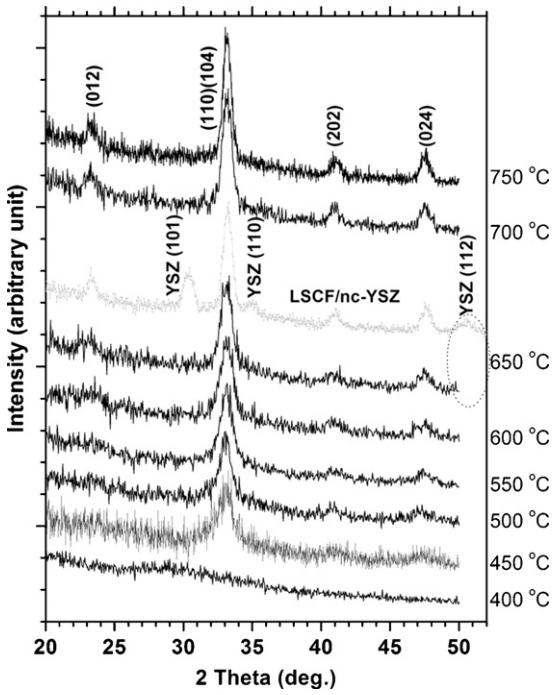

Fig. 1. XRD patterns (black lines) of amorphous LSCF/sc-YSZ thin films annealed at 400 °C, 450 °C, 500 °C, 550 °C, 600 °C, 650 °C, 700 °C, and 750 °C. Light gray lines are XRD patterns taken from LSCF/nc-YSZ-film annealed at 650 °C.

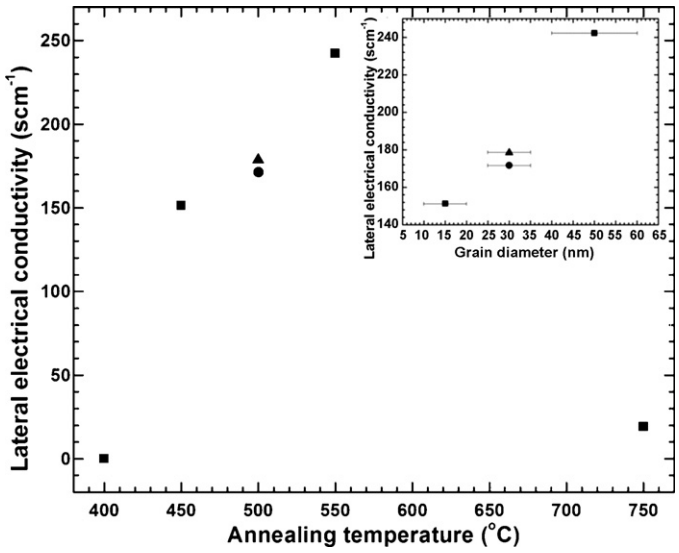

Fig. 2. RT conductivity of amorphous LSCF/sc-YSZ thin films annealed sequentially (square symbols) at 400 °C, 450 °C, 550 °C, and 750 °C. Circular and triangular symbols represent LSCF/sc-YSZ thin films annealed directly at 500 °C for 2 h and 20 h, respectively. Inset on the upper right displays electrical conductivity as a function of grain diameter, whose range is indicated by error bars, for 450 °C, 500 °C, and 550 °C annealed LSCF/sc-YSZ thin films.

at 450 °C and they become more discernible at higher annealing temperatures. Compared to rhombohedral $La_{0.6}Sr_{0.4}C_{0.8}F_{0.2}O_3$ (JCPDS 48-0124 [26]), the 33.1° peak is identified as the superposition of (1 1 0) and (1 0 4) peaks, while the 23.1°, 40.7° and 47.2° peaks represent (1 0 0), (2 0 2) and (0 2 4) peaks, respectively. Note that relative intensity of the peaks is in agreement with reported X-ray data for LSCF bulk crystals with identical composition [27]. As seen in Fig. 1, these four characteristic LSCF peaks can be clearly seen in 650 °C annealed 54 nm LSCF films on nanocrystalline YSZ films that were deposited on Si_3N_4-coated Si substrates (referred to as LSCF/nc-YSZ thin films). Note that for the LSCF/nc-YSZ thin films, YSZ (1 0 1) peak at ~30.0°, (110) peak at ~35.0°, and (1 1 2) peak at ~50.5° (JCPDS 30-1468 [28]) are also visible.

Fig. 2 shows RT conductivity as a function of annealing temperature for the films annealed at 400 °C, 450 °C, 500 °C, 550 °C, and 750 °C – note that circular and triangular symbols are for annealing time study at 500 °C, and is discussed further below. The crystallization is also evident from the significant increase in room temperature (RT) lateral electrical conductivity (σ) when comparing 450 °C annealed ($\sigma = 151.35\ S\ cm^{-1}$) to 400 °C annealed ($\sigma = 0.03\ S\ cm^{-1}$) LSCF/sc-YSZ thin films. The maximum conductivity ($\sigma = 242.24\ S\ cm^{-1}$) was found for the films annealed at 550 °C. Such high RT electrical conductivity is extremely close to the value reported ($\sigma \sim 267\ S\ cm^{-1}$) in Ref. [23] for macrocrystalline LSCF with the same composition. Electrical conductivity as a function of grain size is shown in the inset of Fig. 2. The result clearly shows that despite affected by nanoscale grains and their boundaries, electrical conductivity is still reasonably high in nanocrystalline LSCF thin films. Although even higher conductivity is expected for the films that were annealed at higher temperatures due to their larger grains, hence less grain boundaries, RT conductivity of 750 °C annealed thin films ($\sigma = 19.12\ S\ cm^{-1}$) is one order of magnitude lower compared to the 550 °C annealed thin films.

To have a better microscopic insight of the annealing-temperature-dependent of conductivity, microstructure evolution

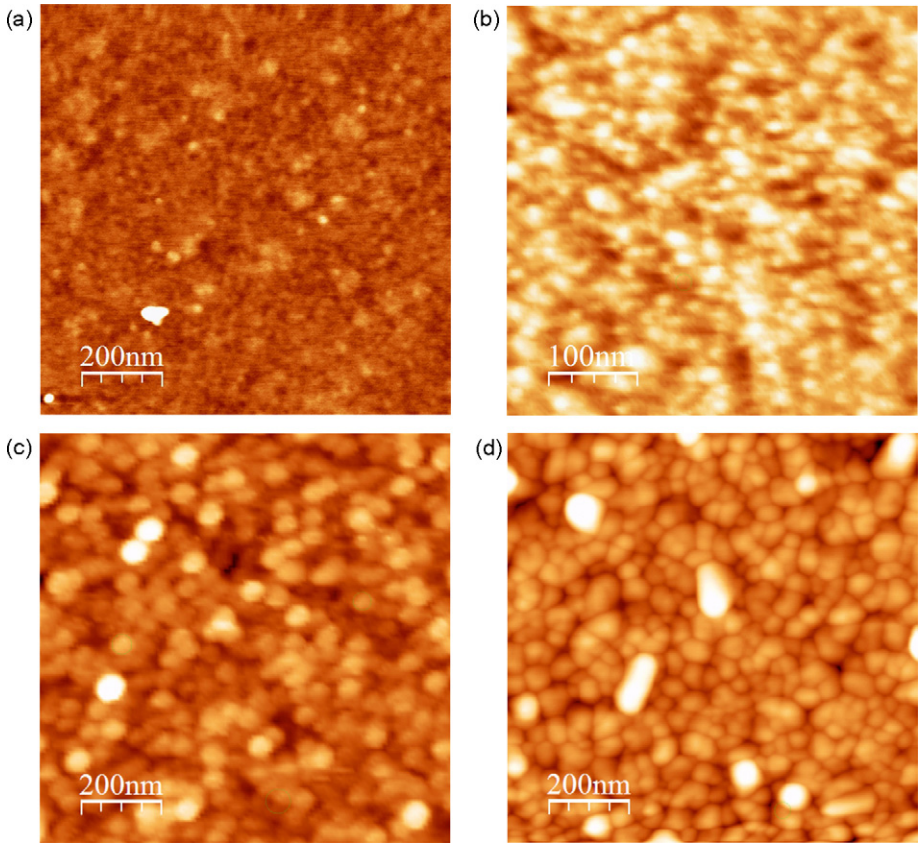

Fig. 3. AFM images taken from LSCF/sc-YSZ thin films annealed at (a) 350 °C, (b) 450 °C, (c) 550 °C, and (d) 750 °C.

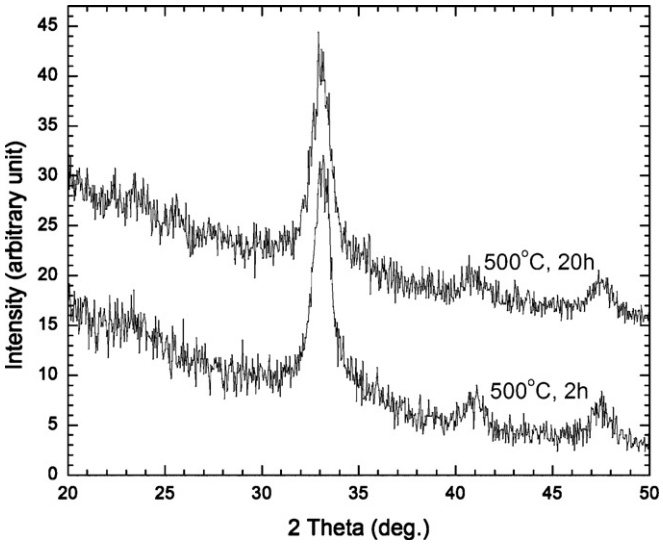

Fig. 4. XRD patterns taken from amorphous LSCF/sc-YSZ thin films annealed directly at 500 °C for 2 h and 20 h, respectively.

of the annealed LSCF/sc-YSZ thin films was investigated by atomic force microscopy (AFM). Fig. 3(a)–(d) show AFM images of LSCF/sc-YSZ thin films that were annealed at 350, 450, 550, and 750 °C, respectively. When the films are amorphous, as seen in Fig. 3(a), the surfaces are very smooth, with root mean square (rms) roughness of 0.24 nm, and no apparent grain microstructures were observed. The thin films annealed at 450 °C, 550 °C, and 750 °C exhibit granular surface morphology as a result of polycrystalline grains. As shown in Fig. 3(b), grains with diameters of 10–20 nm emerge after crystallization at 450 °C. With further annealing to 550 °C, as shown in Fig. 3(c), the grains grow to diameters ranging 40–60 nm with nearly uniform size distribution. Therefore, compared to the 450 °C annealed thin films, the larger grain size leads to higher conductivity in the 550 °C annealed thin films. Annealing at 750 °C, as seen in Fig. 3(d), results in larger grains and a larger variation in grain size due to the coalescence of grains at the expense of small grains. Such grain growth behavior after crystallization is also responsible for the change in rms roughness, which was determined by atomic force microscopy to be 0.49 nm, 1.49 nm, and 3.39 nm for the 450 °C, 550 °C, and 750 °C annealed 54 nm LSCF/sc-YSZ thin films, respectively. The higher rms roughness of 750 °C annealed thin films is also likely a result of aggregation on surfaces. As will be shown in Fig. 9, grain coalescence and aggregation result in loss of intimate contact between some grains and formation of pin holes at some grain junctions. Consequently, it is likely that the discontinuity in microstructure, which inhibits electronic transport, is partially responsible for the observed lower conductivity of the 750 °C annealed thin films.

It is known that the microstructure is also related to annealing time. To investigate its influence, two 54 nm amorphous LSCF/sc-YSZ thin films were deposited concurrently and then annealed at 500 °C for 2 h and 20 h, respectively. It was found, as plotted in Fig. 2, that RT conductivity of both thin films is consistent with the thin films that underwent sequential annealings and 20 h of annealing only slightly increases RT conductivity – namely, 178.47 S cm^{-1} vs. 171.71 S cm^{-1} for the 20-h and 2-h annealed thin films, respectively. The result is attributed to similar crystallinity and grain size of these two thin films and indicates that, to produce noticeable grain size change, a much longer annealing time is needed. As seen in Fig. 4, XRD patterns of these two thin films are almost identical. Similar grain size, in 25–35 nm range, is also observed in Fig. 5(a) and (b), which display AFM images of the 2-h and 20-h annealed thin films, respectively.

Effect of substrate temperature on crystallization, microstructure, and RT conductivity of as-deposited LSCF/sc-YSZ thin films was also investigated. Fig. 6 shows XRD patterns of LSCF/sc-YSZ thin films deposited at 400 °C, 450 °C, and 500 °C. Microstructures of the 400 °C, 450 °C, and 500 °C as-deposited LSCF/sc-YSZ thin films are displayed in Fig. 7(a)–(c), respectively. RT conductivity studies of the thin films were also performed and they are 0.35 S cm^{-1} and 0.61 S cm^{-1} for 450 °C as-deposited and 500 °C as-deposited thin films, respectively. As seen in Fig. 6 and from the RT resistivity measurement, initiation of crystallization also takes place in 400–450 °C range, consistent with the effect of annealing temperature shown in Fig. 1. However, it was found that the LSCF (1 0 1) and (1 0 4) peak is located at ~32.2° 2-theta, as opposed to 33.1° 2-theta shown in Fig. 1; LSCF (0 2 4) peak is also shifted to a lower 2-theta. The difference is attributed to the as-deposited LSCF thin films crystallizing in extremely low oxygen partial pressure environment and, hence, possesses greater oxygen non-stoichiometry when compared to air-annealed thin films. The oxygen non-stoichiometry introduces high level of oxygen vacancies. Moreover, to maintain charge neutrality, the loss of oxygen is compensated by Co reduction from Co^{4+} and Co^{3+} to Co^{3+} and Co^{2+} [27]. Due to higher ionic radius in smaller valence Co ions, such charge compensation leads to a larger lattice constant [27] and, subsequently, a smaller XRD peak position. Crystallization behavior of the as-deposited thin films is revealed from AFM images. As seen in Fig. 7(a), no noticeable grain morphology is observed in the 400-°C as-deposited LSCF/sc-YSZ thin films. Fig. 7(b) shows the presence of grain morphology but it is only discernible in some regions. Together with the relatively flat

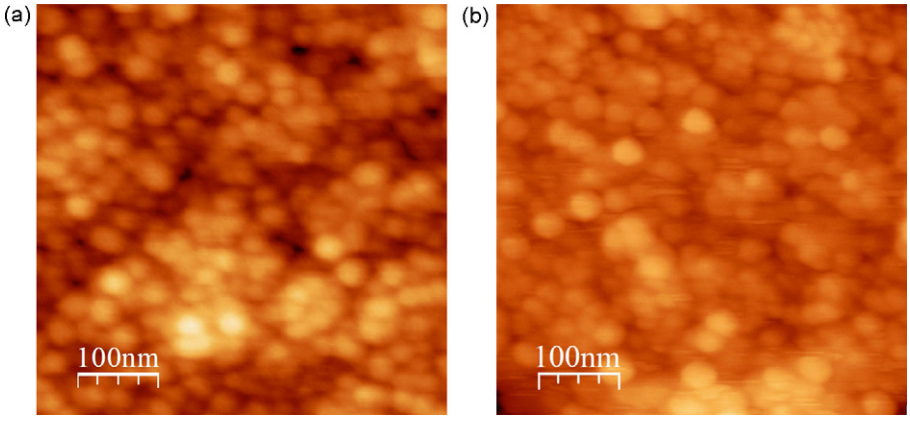

Fig. 5. AFM images taken from LSCF/sc-YSZ thin films annealed directly at 500 °C for 2 h and 20 h, respectively.

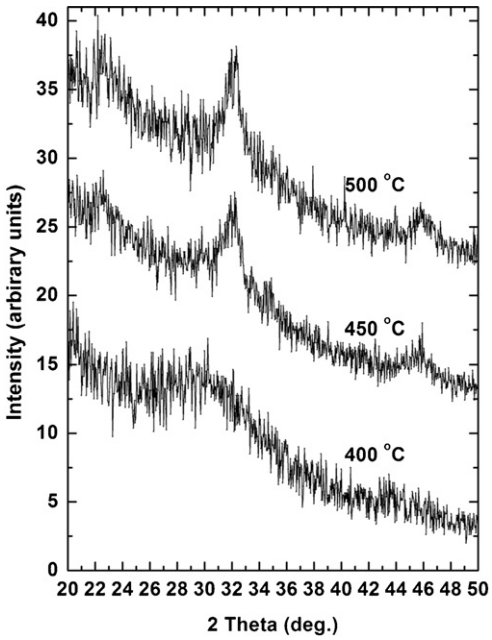

Fig. 6. XRD patterns taken from LSCF/sc-YSZ thin films deposited at 400 °C, 450 °C, and 500 °C.

XRD intensity around 28–31° 2-theta – which is the trace of non-crystallized, 400-°C as-deposited thin films – in Fig. 6; therefore, it is estimated that the 450-°C as-deposited thin film is partially crystallized. When deposited at 500 °C, the film is fully crystallized, as evident in Fig. 7(c), and grain size distribution is fairly uniform. The grain size is in 15–20 nm range, which is similar to that in 450-°C as-deposited thin films but half of that in the 500-°C annealed thin films (Fig. 5.) The difference in degree of crystallization leads to higher conductivity in 500-°C as-deposited thin films. However, compared to the 500-°C annealed thin films, the conductivity is more than two orders of magnitude lower. Such significant low conductivity in the 500-°C as-deposited thin films is likely the combined effect of small grains and high oxygen deficiency. The former introduces more grain boundaries that inhibit electronic transport normal to them, while the latter changes charge compensation mechanism and would not only greatly reduce concentration of holes [27], which are responsible for electronic conductivity, in grain bulk but also traps or eliminates holes when they transport across grain boundaries.

Both annealing and substrate temperature studies show the onset temperature of crystallization, which is in 400–450 °C range, for the LSCF thin films is lower than reported values in literature [4]. This could be partly due to the fact that during sputtering, the energy released after the energetic adatom bombardment greatly promotes ordering of surface atoms locally, albeit at the cost of disordering surface atoms when sputtered species impinge onto the surface. As a result, relatively low annealing or substrate temperature is sufficient to rearrange atoms for the crystallization to occur. The relatively low-temperature treatment also greatly minimizes the interfacial reactions between LSCF and single crystalline YSZ and nanocrystalline YSZ surfaces, as evident in Fig. 1 – in which only LSCF and YSZ peaks are present and XRD peaks of well-known reaction products (namely, $La_2Zr_2O_7$ ad $SrZrO_3$) are absent [17]. In contrast, conventional spray coating, screen printing, or tape casting methods require higher temperature treatment and tend to

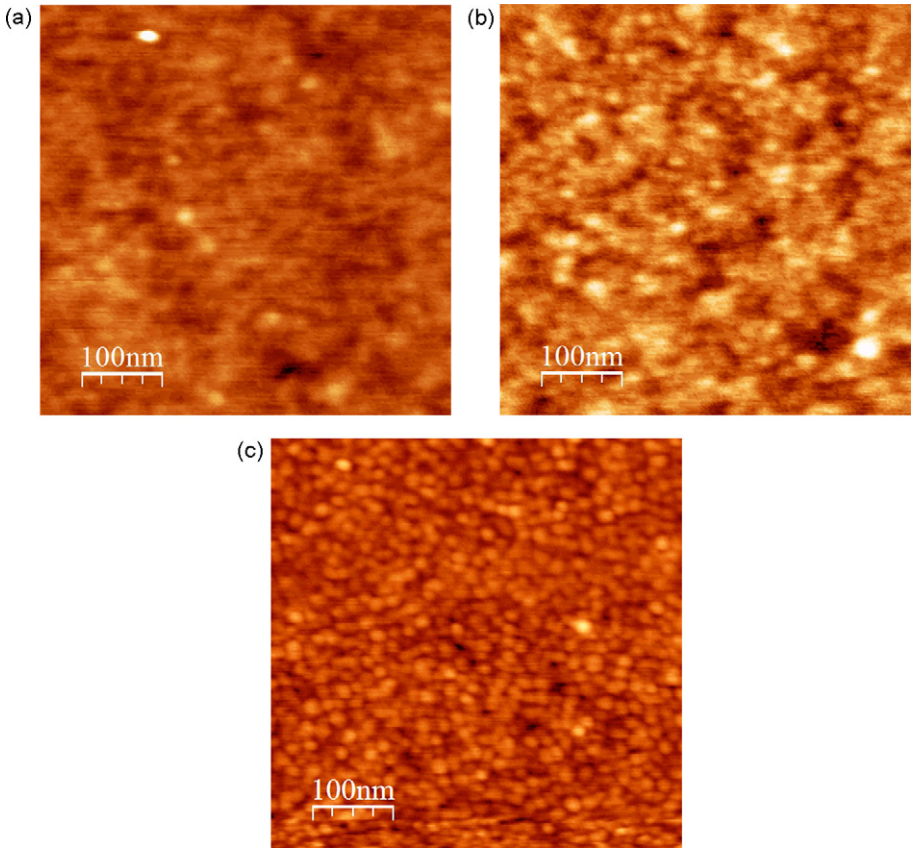

Fig. 7. AFM images taken from LSCF/sc-YSZ thin films deposited at 400 °C, 450 °C, and 500 °C.

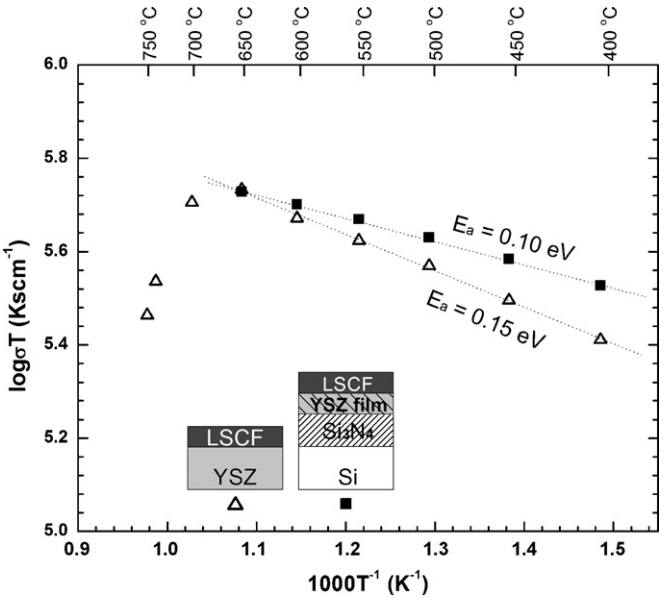

Fig. 8. Arrhenius plot of product of in-plane electrical conductivity and temperature for LSCF/sc-YSZ (△) and LSCF/nc-YSZ (■) thin films. The corresponding layer structure and symbol for each film are illustrated on the bottom of the figure. Inset on the upper right is an XRR pattern taken from LSCF/sc-YSZ thin films.

form reaction layers with thicknesses of tens of nm between LSCF and YSZ [17,19]. Although a ceria interlayer can be used to avoid interfacial reactions, it suffers from stability under low oxygen partial pressures [19].

Fig. 8 shows an Arrhenius plot of product of lateral electrical conductivity, σ, and temperature, T, as function of reciprocal temperature for the LSCF/sc-YSZ and LSCF/nc-YSZ thin films. Deposition time is the same for both LSCF thin films and quantitative analysis of the X-ray reflectivity pattern taken from the LSCF/sc-YSZ thin films (displayed as an inset) indicates their film thickness is ~54 nm. Prior to the measurement, the LSCF/sc-YSZ thin films were annealed at 750 °C, while LSCF/nc-YSZ thin films were annealed at 650 °C for 5 h to stabilize the microstructures. Note that since YSZ single crystal is not an electronic conductor under the conditions reported here and has ionic conductivity nearly three orders of magnitude lower [1] than the measured lateral electrical conductivity, the measured lateral electrical conductivity should primarily represent the total electronic and ionic conductivity of the LSCF thin films. Furthermore, since electronic conductivity of LSCF is three orders or magnitude higher than its ionic conductivity [14], it is reasonable to assume that the measured lateral electrical conductivity represents contribution from LSCF and its adjacent surfaces/interfaces.

After the measurement, surface morphologies of the same films were investigated by SEM. Figs. 9(a) and 4(b) show the SEM images of LSCF/sc-YSZ and LSCF/nc-YSZ thin films, respectively. Compared to Fig. 3(d) – for which the films were annealed at 750 °C for 2 h, crystallites larger than 100 nm are formed on the surface of LSCF/sc-YSZ thin films. It is likely due to further coalescence of grains during the additional annealing time (5 h) prior to the measurement. As seen in Fig. 9(a), LSCF/sc-YSZ thin films are crack-free. However, some of the grains and grain junctions are not in intimate contact. In contrast, the grains in the LSCF/nc-YSZ thin films are all in close contact. However, due to the large thermal expansion mismatch between $La_{0.6}Sr_{0.4}Co_{0.8}Fe_{0.2}O_{3(\delta}$ (= $\sim 21.2 \times 10^{-6}\,K^{-1}$) [29] and Si (= $\sim 3 \times 10^{-6}\,K^{-1}$), microcracks develop after the 650 °C treatment. Note that such microcracks are only visible in high-resolution SEM images.

As seen in Fig. 8, the temperature dependence of in-plane electrical conductivity in LSCF/sc-YSZ thin films is similar to that of LSCF bulk with the same [27] and similar (namely, $La_{0.8}Sr_{0.2}Co_{0.8}Fe_{0.2}O_{3(\delta}$ in Ref. [14], $La_{0.4}Sr_{0.6}Co_{0.8}Fe_{0.2}O_{3(\delta}$ in Ref. [18], and $La_{0.6}Sr_{0.4}Co_{0.2}Fe_{0.8}O_{3(\delta}$ in Ref. [30]) compositions – namely, lateral electrical conductivity increases with increasing temperature, reaches a maximum, and then decreases with a further increase in temperature. Such behavior is due to the competition between oxygen vacancy ($V_O^{\bullet\bullet}$) charge and hole carrier ($B_B^{\bullet}$) compensation mechanism in LSCF, which possesses ABO_3 perovskite structures. The hole carrier $B_B^{\bullet}$ in LSCF is a result of divalent Sr dopants in trivalent La occupied A sites and lower polaron site energy in B-site cations [14,18].

Below the temperature at which maximum conductivity occurs, i.e., $T < T_{max}$, hole carrier compensation mechanism dominates and lateral electrical conductivity is attributed to thermal activation of small polaron hopping [4,14,18] that is generally expressed by [31]

$$\sigma = \left(\frac{\sigma_0}{T}\right) \exp\left(\frac{-E_a}{k_B T}\right), \quad (1)$$

where σ_0 is conductivity coefficient, k_B is Boltzmann's constant, and E_a is the activation energy [30]. When T is above T_{max}, oxygen vacancy ($V_O^{\bullet\bullet}$) charge compensation mechanism prevails due to the formation of oxygen vacancies [14]. As seen in Eq. (2), each oxygen vacancy creation leads to consumption of two hole carriers.

$$2B_B^{\cdot} + O_O^x \rightarrow V_O^{\cdot\cdot} + 2B_B^x + \tfrac{1}{2}O_2 \quad (2)$$

As a result, when $T > T_{max}$, lateral electrical conductivity that arises from thermally activated polarons decreases rapidly. Such phenomenon is well known in LSCF bulk crystals [14,18,27].

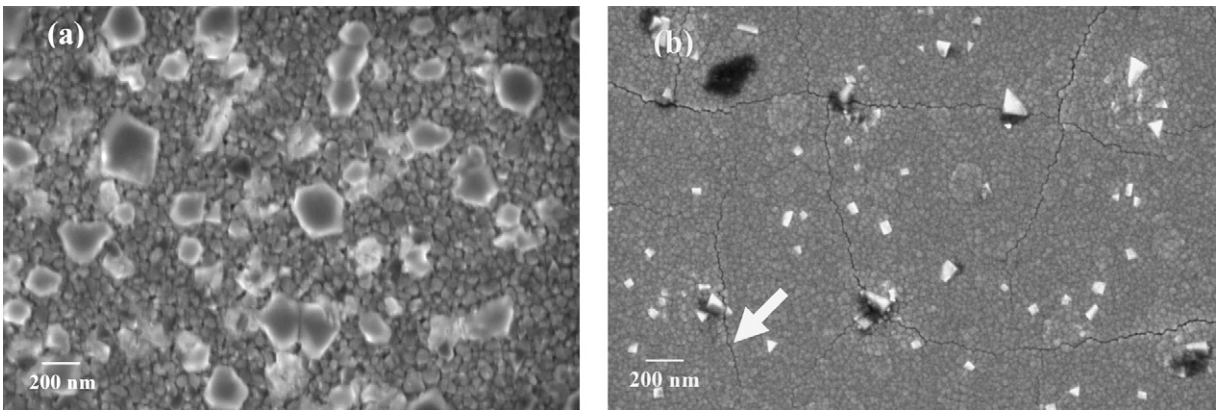

Fig. 9. SEM images of (a) LSCF/sc-YSZ and (b) LSCF/nc-YSZ thin films after high temperature electrical conductivity measurement. A representative microcrack in (b) is indicated by an arrow on the lower left.

Following Eq. (1), E_a for LSCF/sc-YSZ and LSCF/nc-YSZ thin films is 0.15 eV and 0.10 eV, respectively, in 650–400 °C range. The E_a of these films is comparable to that reported for $La_{0.4}Sr_{0.6}Co_{0.8}Fe_{0.2}O_{3(\delta}$ (E_a = 0.17 eV) [18] and $La_{0.8}Sr_{0.2}Co_{0.8}Fe_{0.2}O_{3(\delta}$ (E_a = 0.08 eV [14].) Compared to LSCF bulk of identical composition [21,27], the maximum electrical conductivity in the LSCF/sc-YSZ and LSCF/nc-YSZ thin films, which is ~580 S cm^{-1} at 650 °C for both films, is lower by a factor of ~2. Although it has been reported that the nanocrystallinity in porous LSCF ultra-thin films may degrade the lateral electrically conductivity by more than one order of magnitude [4], our result shows that the relatively low level of porosity in sputtered thin films as evident from the microstructural characterization, could compensate the adverse effect of nanocrystallinity and maintain high lateral electrical conductivity in nanocrystalline LSCF ultra-thin films. The slight difference in E_a and σ for the LSCF/sc-YSZ and LSCF/nc-YSZ thin films is likely related to their microstructures. In general, LSCF with lower porosity and larger grains tends to possess lower activation energy and high electrical conductivity [4,32]. Therefore, the porosity-free microstructures in LSCF/nc-YSZ thin films could be responsible for the lower E_a and higher lateral electrical conductivity when compared to LSCF/sc-YSZ thin films.

Despite the fact that E_a and σ in our sputtered LSCF thin films are comparable to those of bulk, T_{max} (= 650 °C) observed in LSCF/sc-YSZ thin films is much higher than that in $La_{0.6}Sr_{0.4}Co_{0.8}Fe_{0.2}O_{3(\delta}$ bulks, T_{max} = 100–350 °C [27] – note to prevent electrical conductivity decrease due to microcracks, the LSCF/nc-YSZ thin films were only measured up to 650 °C and the result indicates their T_{max} is also likely greater than 650 °C. Similar observation has also been reported in nanocrystalline, ultra-thin $La_{0.6}Sr_{0.4}Co_{0.2}Fe_{0.8}O_{3(\delta}$ films (T_{max} > 800 °C) [4] when comparing to $La_{0.6}Sr_{0.4}Co_{0.2}Fe_{0.8}O_{3(\delta}$ bulk, T_{max} = 500–700 °C [14]. Such result is interesting since higher free surface/volume ratio in nanocrystalline, ultra-thin films would promote the formation of oxygen vacancies – because of increased surface area for oxygen molecules, according to Eq. (2) – and, thus, lower T_{max}. We speculate that the inherent higher oxygen vacancy concentration or the capability of accommodating higher concentration of oxygen vacancies in grain boundaries of the nanocrystalline thin films might require higher level of oxygen vacancies, hence, higher temperature, for the reaction in Eq. (2) to proceed. Moreover, since the formation of oxygen vacancies is accompanied by the expansion of unit cell volume [14,27], the mechanical constraints imposed by substrates, that do not allow LSCF thin films to expand freely, could also possibly contribute to the experimentally observed higher T_{max}.

Although the sputtered LSCF thin films exhibit excellent crystallinity and high electrical conductivity, our initial attempts to fabricate μSOFCs using thick (>55 nm) LSCF films on 75 nm YSZ electrolyte thin films were not successful because the presence of microcracks (as seen in Fig. 9(b)) causes failures of LSCF-YSZ membranes (as shown in Fig. 10(a)) after releasing from Si_3N_4 and Si substrates or during measurement when temperature is above 300 °C. It is known that tensile stresses (driving force for the microcracks) in high melting temperature, polycrystalline thin films are thickness dependent and thinner films tend to have lower magnitude of stresses [33]. Hence, microcracks and failures of μSOFC membranes were prevented by depositing 15 nm LSCF on 75 nm YSZ thin films. The crack-free microstructures of the 15 nm LSCF on a LSCF/YSZ/Pt membrane is evident in Fig. 10(b), taken after performing fuel cell measurement, and the intact membrane after the measurement can be seen in Fig. 10(c). Such an approach enabled us to demonstrate μSOFCs that use nanocrystalline LSCF ultra-thin films as cathodes for the first time. Power density as high as 60 mW cm^{-2} and 25 mW cm^{-2} have been achieved when measured at 500 °C and 450 °C, respectively. Complete fabrication details of fuel cell micro-devices and variable temperature performance will be reported elsewhere [34]. These results indicate that nanocrystalline, ultra-thin LSCF films are promising for low- or intermediate-temperature SOFC cathode applications and, to further improve the performance of μSOFCs, it is important to optimize the microstructures of LSCF and YSZ thin films and understand the thickness- and temperature-dependent properties of LSCF thin films.

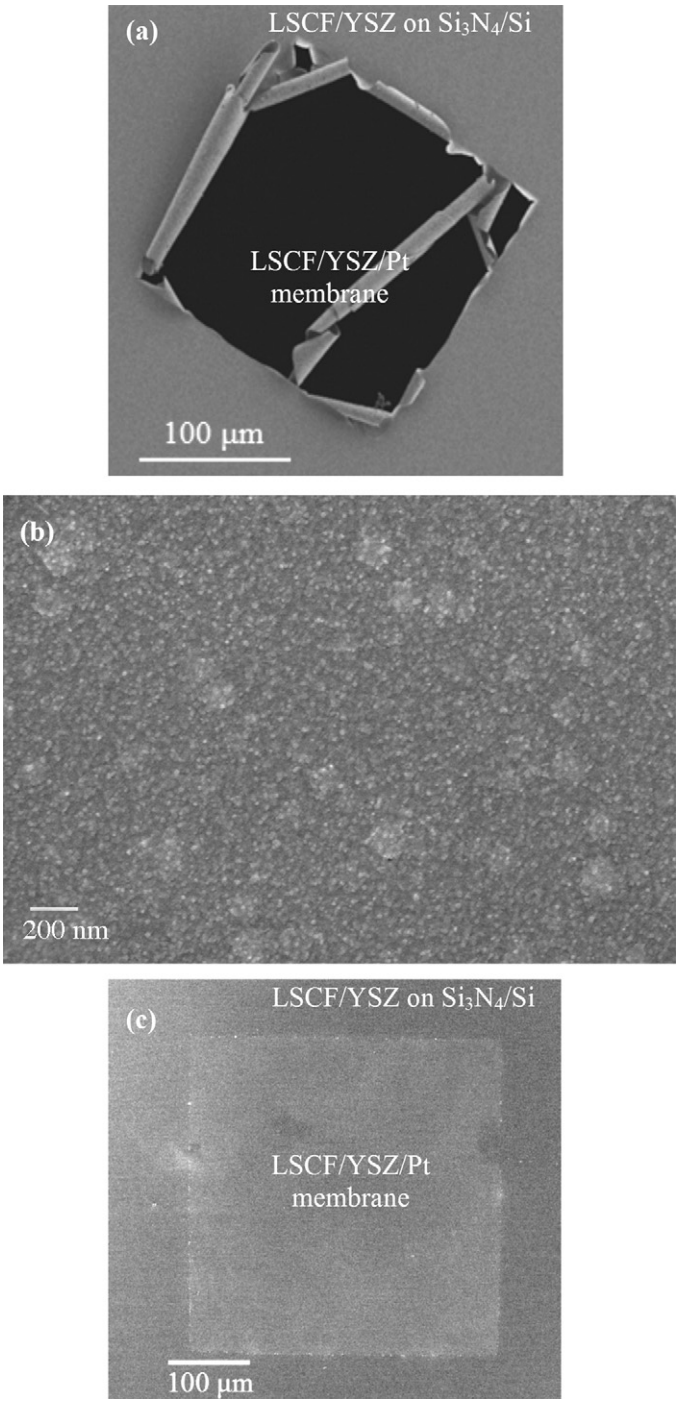

Fig. 10. SEM images of (a) a 650 °C annealed 54 nm-LSCF/75 nm-YSZ/Pt membrane, (b) surface morphology of 15 nm LSCF thin films in a 650 °C annealed 15 nm-LSCF/75 nm-YSZ/Pt membrane, and (c) a 650 °C annealed 15 nm-LSCF/75 nm-YSZ/Pt membrane.

4. Conclusions

In conclusion, we have demonstrated for the first time that RF sputtering provides a low-temperature synthesis route to deposit $La_{0.6}Sr_{0.4}Co_{0.8}Fe_{0.2}O_{3(\delta}$ thin films. The sputtered LSCF thin films exhibit good crystallinity and absence of interfacial reaction products. High lateral electrical conductivity of $\sim$580 S cm^{-1} at 650 °C has been obtained for LSCF/nc-YSZ and LSCF/sc-YSZ thin films; while activation energies for conductivity were determined to be 0.15 eV and 0.10 eV, respectively, in the range of 650–400 °C. μSOFCs using 15 nm nanocrystalline LSCF as cathodes have been demonstrated to achieve a peak power density of 60 mW cm^{-2} at 500 °C. The results indicate that nanocrystalline LSCF ultra-thin films hold potential for intermediate- and low-temperature SOFC cathodes.

Acknowledgment

The authors acknowledge funding from SiEnergy Systems, Harvard University Center for Environment for financial support.

References

[1] B.C.H. Steele, A. Heinzel, Nature 414 (2001) 345–352.
[2] S.C. Singhal, K. Kendall, High Temperature Solid Oxide Fuel Cells: Fundamentals, Design and Applications, Elsevier Advanced Technology, Oxford, UK, 2003.
[3] H. Huang, M. Nakamura, P. Su, R. Fasching, Y. Saito, F.B. Prinz, J. Electrochem. Soc. 154 (2007) B20–B24.
[4] D. Beckel, Ph.D. Thesis, Thin Film Cathode for micro Solid Oxide Fuel Cell, Swiss Federal Institute of Technology, Zurich, 2007.
[5] J.L. Hertz, H.L. Tuller, J. Electrochem. Soc. 154 (2007) B413–B418.
[6] D. Beckel, D. Briand, A. Bieberle-Hütter, J. Courbat, N.F. de Rooij, L.J. Gauckler, J. Power Sources 166 (2007) 143–148.
[7] J.W. Fergus, JOM December 59 (2007) 56–62.
[8] J. Fleig, Annu. Rev. Mater. Res. 33 (2003) 361–382.
[9] R. O'Hayre, S.W. Cha, W. Colella, F.B. Prinz, Fuel Cell Fundamentals, John Wiley & Sons, New York, USA, 2005.
[10] I. Yasuda, K. Ogasawara, M. Hishinuma, T. Kawada, M. Dokiya, Solid State Ionics 86–88 (1996) 1197–1201.
[11] Z. Shao, S.M. Haile, Nature 431 (2004) 170–173.
[12] W.G. Wang, M. Mogensen, Solid State Ionics 176 (2005) 457–462.
[13] M. Prestat, J.-F. Koenig, L.J. Gauckler, J. Electroceram. 18 (2007) 111–120.
[14] L.-W. Tai, M.M. Nasrallah, H.U. Anderson, D.M. Sparlin, S.R. Sehlin, Solid State Ionics 76 (1995) 259–271.
[15] F.S. Baumann, J. Fleig, G. Cristiani, B. Stuhlhofer, H.-U. Habermeier, J. Maier, J. Electrochem. Soc. 154 (2007) B931–B941.
[16] S.B. Adler, J.A. Lane, B.C.H. Steele, J. Electrochem. Soc. 143 (1996) 3554–3564.
[17] W.-H. Kim, H.-S. Song, J. Moon, H.-W. Lee, Solid State Ionics 177 (2006) 3211–3216.
[18] H.Y. Tu, Y. Takeda, N. Imanishi, O. Yamamoto, Solid State Ionics 117 (1999) 277–281.
[19] H. Yokokawa, N. Sakai, T. Horita, K. Yamaji, M.E. Brito, Mater. Res. Soc. Bull. 30 (2005) 591–595.
[20] A. Mai, V.A.C. Haanappel, F. Tietz, D. Stover, Solid State Ionics 177 (2006) 2103–2107.
[21] Y. Teraoka, T. Nobunaga, K. Okamoto, N. Miura, N. Yamazoe, Solid State Ionics 48 (1991) 207–212.
[22] A. Bieberle-Hutter, H.L. Tuller, J. Electroceram. 16 (2006) 151–157.
[23] Y. Teraoka, H.M. Zhang, K. Okamoto, N. Yamazoe, Mater. Res. Bull. 23 (1988) 51–58.
[24] J.W. Stevenson, T.R. Armstrong, R.D. Carneim, L.R. Pederson, W.J. Weber, J. Electrochem. Soc. 143 (1996) 2722–2729.
[25] A. Karthikeyan, C.L. Chang, S. Ramanathan, Appl. Phys. Lett. 89 (2006) 183116.
[26] ICDD-JCPDS card no. 48-0124.
[27] S. Wang, M. Katsuki, M. Dokiya, T. Hashimoto, Solid State Ionics 159 (2003) 71–78.
[28] ICDD-JCPDS card no. 30-1468.
[29] H. Ullmann, N. Trofimenko, F. Tietz, D. Stover, A. Ahmad-Khanlou, Solid State Ionics 138 (2000) 79–90.
[30] G.Ch. Kostogloudis, Ch. Ftikos, Solid State Ionics 126 (1999) 143–151.
[31] E. Iguchi, K. Ueda, W. Jung, Phys. Rev. B 54 (1996) 17431–17437.
[32] A. Esquirol, N.P. Brandon, J.A. Kilner, M. Mogensen, J. Electrochem. Soc. 151 (2004) A1847–A1855.
[33] F. Spaepen, Acta Mater. 48 (2000) 31–42.
[34] A.C. Johnson, B.K. Lai, H. Xiong, S. Ramanathan, J. Power Sources, (2008), in press, doi:10.1016/j.jpowsour.2008.10.021.